Article

One-Step Self-Assembly Synthesis α-Fe$_2$O$_3$ with Carbon-Coated Nanoparticles for Stabilized and Enhanced Supercapacitors Electrode

Yizhi Yan [ID]**, Haolin Tang *, Fan Wu, Rui Wang** [ID] **and Mu Pan**

State Key Laboratory of Advanced Technology for Material Synthesis and Processing,
Wuhan University of Technology, Wuhan 430070, Hubei, China; yanyizhi2005@163.com (Y.Y.);
wu_fan@whut.edu.cn (F.W.); 512651259@whut.edu.cn (R.W.); panmu@whut.edu.cn (M.P.)
*   Correspondence: thln@whut.edu.cn; Tel.: +86-27-8788-4448; Fax: +86-27-8787-9468

Abstract: A cocoon-like α-Fe$_2$O$_3$ nanocomposite with a novel carbon-coated structure was synthesized via a simple one-step hydrothermal self-assembly method and employed as supercapacitor electrode material. It was observed from electrochemical measurements that the obtained α-Fe$_2$O$_3$@C electrode showed a good specific capacitance (406.9 Fg^{-1} at 0.5 Ag^{-1}) and excellent cycling stability, with 90.7% specific capacitance retained after 2000 cycles at high current density of 10 Ag^{-1}. These impressive results, presented here, demonstrated that α-Fe$_2$O$_3$@C could be a promising alternative material for application in high energy density storage.

Keywords: one-step; self-assembly; α-Fe$_2$O$_3$; carbon coating; supercapacitors

1. Introduction

With the development of the economy, environmental pressure has been increasing, and it is very urgent to develop a new, low cost, environmentally friendly alternative energy source and energy storage system [1–4]. Supercapacitors are considered to be a promising candidate material for energy storage because of their advantages of high power density, excellent rate capacitance, long cycle life, and so on [5–7]. The supercapacitor can be classified into two categories: electric double-layer capacitors and pseudocapacitors. The charge storage capacitance in the double-layer capacitors is derived from the electrostatic forces based on the electrical double layers. While it is derived from the rapid Faraday oxidation-reduction reaction in the pseudocapacitors [8]. Electrode material is the main factor in determining the performance of supercapacitors [9]. Due to the varied oxidation states for efficient redox charge transfer and high theoretical specific capacitance, transition metal oxides have been considered to be one of the most attractive electrode materials for supercapacitors [10,11]. Hematite (Fe$_2$O$_3$), a typical transition metal oxide, has attracted a lot of attention for application in supercapacitors due to its low cost, environmental friendliness, and many other advantages [12–14]. However, Fe$_2$O$_3$ electrode material also exhibits some serious disadvantages, such as poor electrical conductivity and large volume change, impeding their commercial applications [15]. Carbon-based materials, thanks to their high electrical conductivity, excellent chemical stability, and superior mechanical properties, can be composited with Fe$_2$O$_3$ to overcome the above-mentioned shortcomings and improve electrochemical property in supercapacitors [16,17]. The coating carbon can increase the electronic conductivity of the matrix material and function as a structural buffering layer to cushion the mechanical stress caused by the large volume change during the cycling process. The coating carbon is able to improve the electrical conductivity of the matrix material and also plays as a constraint layer to buffer the cycle of large volume expansion in the charge and discharge process.

In this work, α-Fe$_2$O$_3$ with a novel carbon-coated structure nanoparticle composite was fabricated via a facile one-step self-assembly synthesis method and employed as electrode for supercapacitors. The α-Fe$_2$O$_3$@C nanoparticles exhibited excellent charge storage properties in terms of high capacitance, superior rate capability, and good cyclic stability. This unique structure is conducive to getting over the above-mentioned shortcomings of Fe$_2$O$_3$. As a result, the performance of composite materials as supercapacitors electrode could be enhanced to some extent. Therefore, the cocoon-like α-Fe$_2$O$_3$ nanoparticles with a novel carbon-coated structure have great potential for practical application in the energy storage field.

2. Experimental Section

2.1. Synthesis of α-Fe$_2$O$_3$@C Composite

All of the chemicals were analytical grade and used as received. At first, 0.06 mol Ferric chloride (FeCl$_3$·6H$_2$O) was dissolved in distilled water to form saturated FeCl$_3$ solution. Then, the saturated FeCl$_3$ solution was slowly dropped into 100 mL boiling deionized water under continuous magnetic stirring. In this process, Fe^{3+}-containing solution was hydrolyzed to Fe(OH)$_3$ colloid with negative charge and presented evident Tyndall phenomenon. After several minutes, 10 mL Poly dimethyl diallyl ammonium chloride ((C$_8$H$_{16}$ClN)$_n$, Mw < 100,000, 35 wt %, Aladdin) (PDDA) solution was gradually added into the homogeneous colloid solution with the assist of magnetic stirring continuously for 3 h. The mixture of the two solutions was then sealed in Teflon-lined stainless steel autoclave at 180 °C for 12 h and cooled down to room temperature. PDDA solution is a type of polycation electrolytes with positive charge. Negatively charged Fe(OH)$_3$ colloidal precursors and positively charged organics were self-assembled under the action of Vander Waals molecular force in the hydrothermally reaction procedure. In the boiling water, Fe^{3+} solution was hydrolyzed into Fe(OH)$_3$ colloid. Then, the colloidal particles were decomposed into Fe$_2$O$_3$ in the subsequent hydrothermal reaction. The relevant chemical reactions are shown as follows:

$$\mathrm{Fe^{3+} + 3H_2O \rightarrow Fe(OH)_3 + 3H^+} \tag{1}$$

$$\mathrm{2Fe(OH)_3 \rightarrow Fe_2O_3 + 3H_2O} \tag{2}$$

The resulting suspension solution was centrifuged, and then the precipitate was washed with distilled water and anhydrous ethanol. Finally, the collected precipitate was dried at 80 °C in air followed by carbonization at 350 °C for 2 h under highly pure nitrogen (N$_2$) to obtain α-Fe$_2$O$_3$@C composite powder samples.

2.2. Materials Characterization

The structure of the material was examined by X-ray diffraction (XRD, D8 Advance, Bruker AXS, Karlsruhe, Germany) with Cu Kα radiation (λ = 1.5406 Å) in the range from 5–80°. The X-ray photoelectron spectroscopy (XPS, ESCALAB 250Xi, Thermo Fisher Scientific, Waltham, MA, USA) was conducted with X-ray instrument with an Al Kα = 300.0 eV excitation source.

The morphology of the active as-prepared sample was examined by field emission scanning electron microscope (FESEM, Zeiss Ultra Plus, ZEISS, Oberkochen, Germany) and transmission electron microscopy (TEM, JEM 2100F, JEOL, Tokyo, Japan). The element mapping images were obtained on an energy dispersive X-ray spectrometry (EDS, Oxford Instruments, Abingdon, UK). Thermogravimetric analysis-Differential scanning calorimetry (TG-DSC, STA449F3, NETZSCH, Selb, Germany) was conducted in air from room temperature to 1000 °C with heating rate of 10 °C/min.

Raman spectra (INVIA, Renishaw Co. Ltd., Gloucestershire, UK) were analyzed with 632.5 nm argon ion laser from 100 to 1800 cm^{-1}. Fourier transform infra-red (FTIR) spectra (Nexus, Thermo Nicolet, Madison, WI, USA) were conducted in the spectral ranges of 400–4000 cm^{-1}. The specific surface areas of samples were recorded using nitrogen adsorption-desorption isotherms via

Brunauer-Emmett-Teller (BET, ASAP 2020M, Micromeritics Instrument, Norcross, GA, USA) analysis at 77 K.

2.3. Electrochemical Measurements

All electrochemical measurements were performed on a CHI660E electrochemical workstation in a typical three-electrode system, with platinum foil and Hg/HgO as the counter electrode and reference electrode, respectively, and the electrolyte was 6 M KOH aqueous solution. The electrochemical impedance spectroscopy (EIS) measurements were carried out on an electrochemical workstation (CHI660E, Chenhua Co. Ltd., Shanghai, China), and the frequency of AC impedance ranges from 0.01–106 Hz with 5 mV amplitude.

The working electrode consisted of as-prepared α-Fe_2O_3@C sample, acetylene black and polytetrafluoroethylene (PTFE) solution in a weight ratio of 70:20:10. The mixture was ground into a mash and then pressed into a sheet by a double roller press and punched into small disks with diameter of 1.0 cm. The disks were wrapped in nickel foam by rolling to form a sandwich structure and used as the working electrode. Each working electrode contained about 2.5 mg α-Fe_2O_3@C active material. The preparation process of sandwich structures working electrode was schematic illustrated in Figure 1. Compared with electrode prepared via conventional method in which the slurry was directly coated on the nickel foam, the electrode with the sandwich structure prepared by this method was harder to fall off.
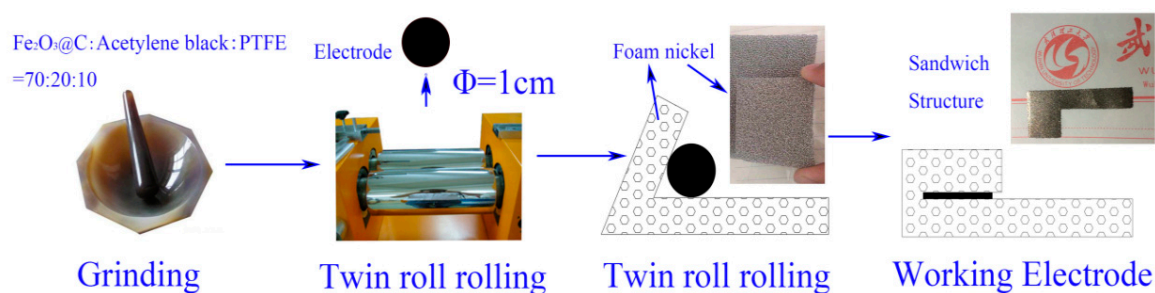

Figure 1. Schematic illustration of preparation of sandwich structure working electrode.

3. Results and Discussion

XRD patterns of α-Fe_2O_3@C samples before and after calcination in N_2 are shown in Figure 2. After calcination, the crystal phase of the samples almost remained unchanged. All obvious diffraction peaks were matched well with the standard α-Fe_2O_3 card (JCPDS No. 33-0664). No impurities phases have been detected and the sample is hexagonal phase α-Fe_2O_3 crystalline structure. No carbon phase peaks have been detected, which indicates that the coated carbon is amorphous. The carbonization temperature under 350 °C is not enough to lead to organic matter graphitization, so the coated carbon layer in this case is in the form of amorphous condition.

As shown in Figure 3a, six Raman scattering peaks are observed at 200–600 cm^{-1} referring to typical hematite [18], which indicates that the iron oxide precursor has been successfully synthesized by a one-step hydrothermal self-assembly process. The D band is associated with disorder carbon, resulting from various types of defects, while G band is associated with the E_{2g} mode of the crystalline graphite [3]. The intensity ratio of D peak and G peak is used to characterize the degree of graphitization of carbon. After calcination, the relative intensity of D peak and G peak is enhanced due to carbonation of organic matter during the calcination process under the high purity N_2. The peaks appeared at ~1320 cm^{-1} and ~1580 cm^{-1} are ascribed to the disordered (D) and graphitic (G) band, respectively. Compared with D peak, the intensity of G peak is very weak, indicating that the coated carbon is mainly in an amorphous state. This result is consistent with the XRD analysis of Figure 2.
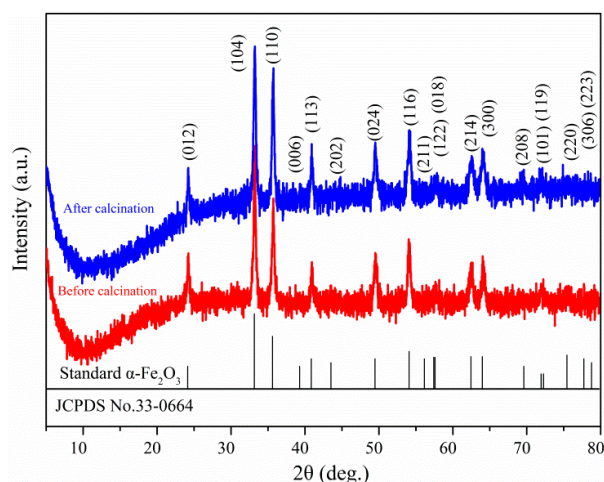
Figure 2. X-ray diffraction (XRD) patterns of α-Fe$_2$O$_3$@C nanoparticle composite before and after calcination.
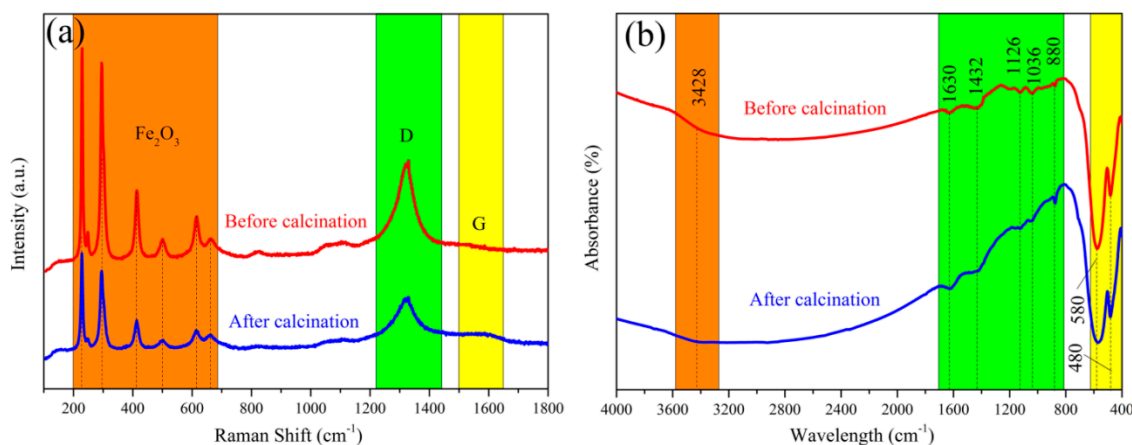

Figure 3. (**a**) Raman spectrums and (**b**) FTIR of α-Fe$_2$O$_3$@C nanoparticle composite before and after calcination.

From Figure 3b, there is a broad absorption peak located at in ~3430 cm^{-1} corresponding to the stretching vibration of hydroxyl (–OH) mode of crystallized water or physically adsorbed water on the material surface. The intensity of this peak decreases after calcination, which result from the loss of some crystalline water caused by the calcination process. The absorption peaks appearing at the ~480 and ~580 cm^{-1} correspond to the Fe–O vibrational mode of typical hematite [19,20]. In the fingerprint peak part (~800–1700 cm^{-1}), the absorption peaks located at 1126, 1432, and 1630 cm^{-1} are attributed to the C–C, C–O, and C=C groups of carbon, respectively [21]. The peaks at 1036 cm^{-1} and 880 cm^{-1} are attributed to the characteristic breathing mode of residual organic matter [22]. After calcination, the relative absorption peak intensity becomes larger. All the above-mentioned absorption bands are matched well with spectroscopic characterizations of typical hematite and amorphous carbon structures, indicating the successful formation of α-Fe$_2$O$_3$@C composite via one-step self-assembly method. This result is in agreement with the XRD and Raman analysis results presented above.

As shown in Figure 4, the α-Fe$_2$O$_3$@C sample presents uniform cocoon-like oval spheres with small particle size of ~500 nm in diameter and ~1 μm in length. The particles are distributed evenly without agglomeration. It is worth noting that α-Fe$_2$O$_3$@C sample clearly reveals its hollow pore structure on the surface (Figure 4c), which can effectively buffer the volume change of Fe$_2$O$_3$. This pore

structure provides a high specific surface and more active sites and increases the electronic conduction for energy storage [23].
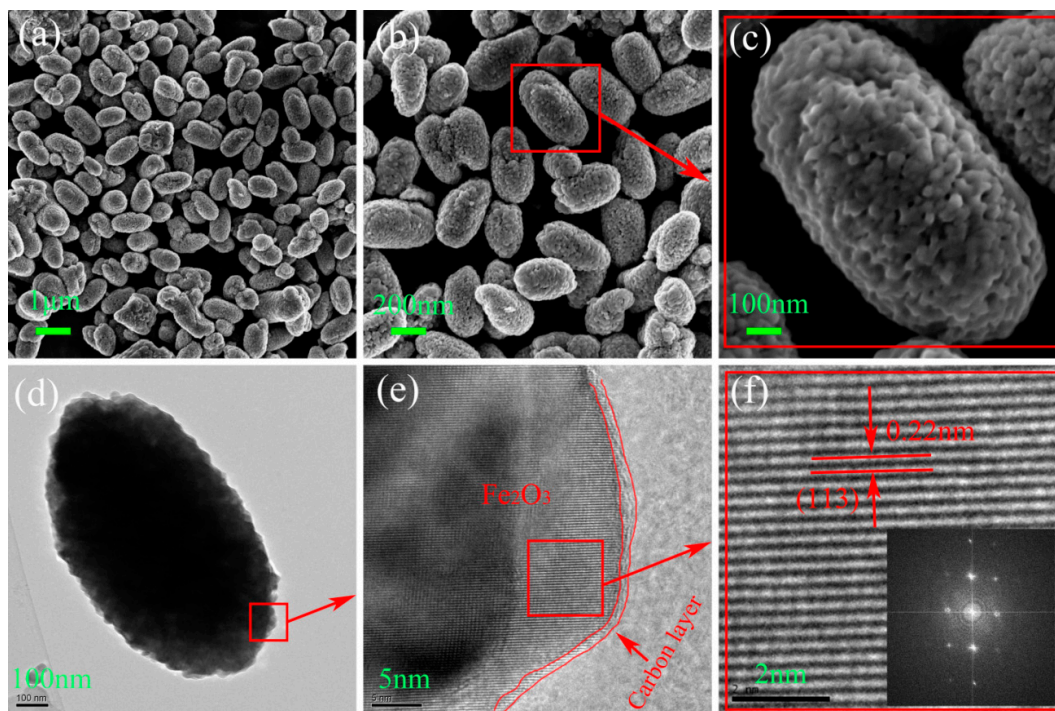

Figure 4. (**a**–**c**) field scanning electron microscopy (FESEM) and (**d**–**f**) transmission electron microscopy (TEM) images of α-Fe$_2$O$_3$@C nanoparticle composite. The insert is the selected area electron diffraction (SAED) image.

TEM was employed to further investigate the microstructures of the α-Fe$_2$O$_3$@C sample. As shown in Figure 4d, there is a light colored coating layer in the edge of the cocoon-like oval ball. With clear lattice fringes, the α-Fe$_2$O$_3$@C samples present typical crystalline structure of α-Fe$_2$O$_3$. While, no lattice fringes are observed in the coating layer of the edge of α-Fe$_2$O$_3$, indicating that the coating layer is amorphous carbon. The uniform and continuous coating layer has a thickness of a few nanometers (Figure 4e).

The HRTEM images (Figure 4f) display a set of parallel fringes with the space separation of 0.22 nm, corresponding to the (113) plane of crystalline α-Fe$_2$O$_3$ (JCPDS No. 33-0664). The selected area electron diffraction (SAED) image (the insert in Figure 4f) indicates that the α-Fe$_2$O$_3$@C sample has a perfect crystal structure. In the α-Fe$_2$O$_3$@C nanocomposites, the carbon coating layer not only serves as a conductive network but also prevents iron oxide particles from volume variation, which is crucial in improving the performance of Fe$_2$O$_3$ electrode [24].

The EDS element mapping of the α-Fe$_2$O$_3$@C sample was also studied. In order to avoid carbon pollution, the powder samples were ultrasonically dispersed in an ethanol solution, dropping on aluminum foil for test. The Fe, O and C elements are found and distributed evenly in the surface of cocoon-like nanospheres (Figure 5b). The signal of C comes from the carbon-coated layers formed during the calcination process with the organic material PDDA, demonstrating that carbon is successfully coated on the Fe$_2$O$_3$ surfaces. As shown in Figure 5f, the Al peak is derived from aluminum foil, and the carbon weight fraction in α-Fe$_2$O$_3$@C sample was about 4.09%. The quality ratio of iron and oxygen element is 66.33% and 29.58%, respectively, agreeing well with the composition ratio of iron oxide.

In order to determine the weight fraction of carbon coated in the α-Fe$_2$O$_3$@C sample more accurately, TG-DSC analysis was conducted. As shown in Figure S1, the carbon quality content in

α-Fe$_2$O$_3$@C sample was about 3.91%, which was almost the same as the result of EDS elemental analysis in Figure 5f. These analyses indicate that carbon has been ideally grown on the surface of Fe$_2$O$_3$ and the amount of the coating carbon is about 4.0%.
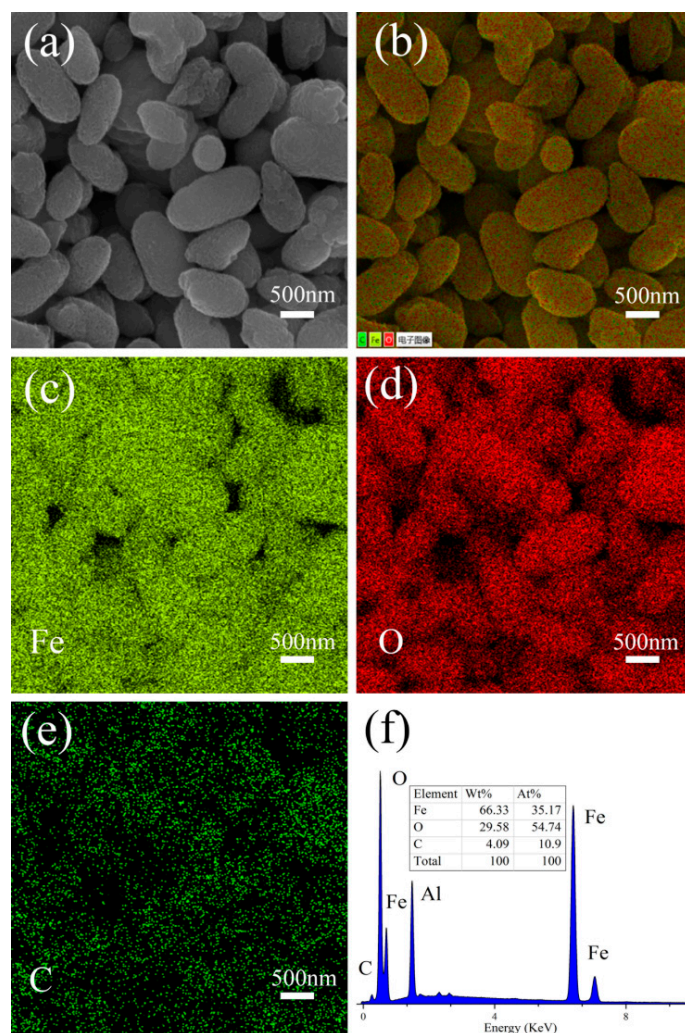

Figure 5. Energy dispersive X-ray spectrometry (EDS) element mapping of α-Fe$_2$O$_3$@C nanoparticle composite. (**a**) The original FESEM images; (**b**) the total element mapping; (**c**) the Fe Kα1 mapping; (**d**) the O Kα1 mapping; (**e**) the C Kα1 mapping; (**f**) the EDS spectra of α-Fe$_2$O$_3$@C nanoparticle.

The XPS analysis was further employed to determine the chemical compositions and bonding conditions of α-Fe$_2$O$_3$@C nanoparticle composite. One can observe clearly the peaks of Fe2p at ~720 eV, C1s peak at 285.0 eV and O1s peak at 530.5 eV from the full-range XPS survey (Figure 6a). The high-resolution spectra of Fe2p, O1s and C1s were plotted in Figure 6b–d, respectively. The Fe2p$_{1/2}$ and Fe2p$_{3/2}$ peaks were observed at 710.8 eV and 724.4 eV, respectively, with the binding energy deference is 13.6 eV. There are two typical satellite peaks (719.3 and 732.3 eV) near the main peak, indicating that iron exists as a trivalent form of Fe^{3+} [25–27].

In Figure 6c, the O1s binding energy is 530.0 eV, corresponding to the typical binding energy of Fe–O bonding, while the peak at 531.3 eV is assigned to C–O, C=O, and O=C–O bonds [28,29]. In Figure 6d, C1s peak can be best fit with four components which is matched well with C sp^2 (C=C, 284.1 eV), C sp^3 (C–C, 284.6 eV), C–O (285.7 eV), and C=O (288.5 eV) [30]. The C sp^2 and C sp^3 peaks represent graphitized carbon and amorphous carbon, respectively [31]. The C sp^3 peak content is 77.9%, indicating that the coating carbon on α-Fe$_2$O$_3$ surface mainly exists in the form of amorphous carbon.
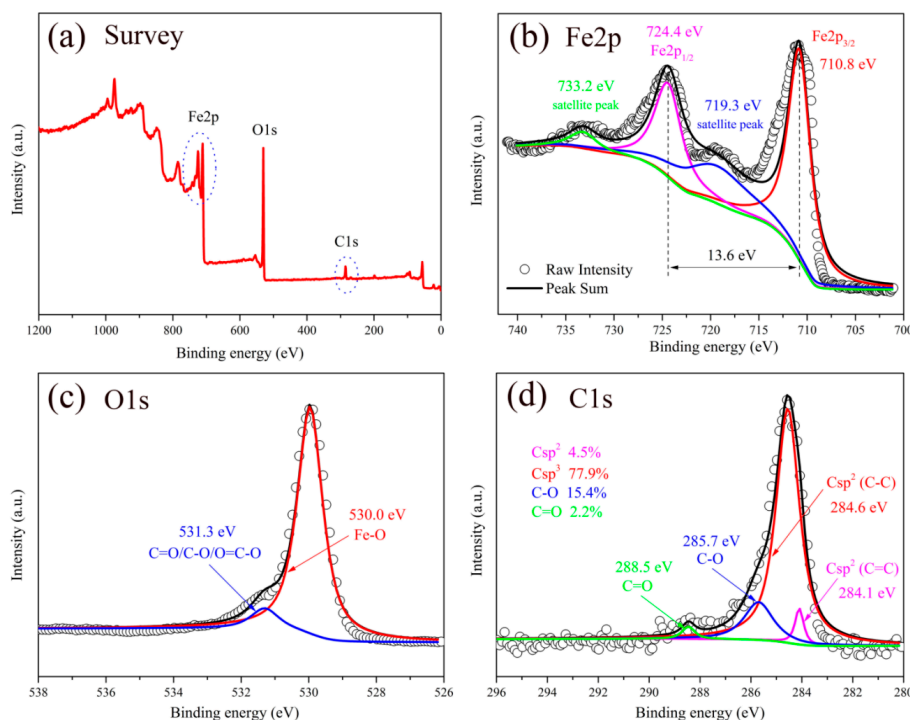
Figure 6. X-ray photoelectron spectroscopy (XPS) spectrum of α-Fe$_2$O$_3$@C nanoparticle composite. (**a**) The full-range XPS survey and the high-resolution spectrum of (**b**) Fe2p, (**c**) O1s and (**d**) C1s.

The specific surface area of the nanoparticles samples was calculated by the BET method with Nitrogen adsorption-desorption isotherms. The Nitrogen adsorption-desorption isotherms of α-Fe$_2$O$_3$@C composite exhibit type IV characteristics, which indicate the presence of mesoporous in the sample [32]. As shown in Figure 7, the corresponding pore size distributions are estimated by the Barrett-Joyner-Halenda (BJH) method. The average pore diameters and pore volume are estimated to be ~17 nm and ~0.0001 cm^3 g^{-1} nm^{-1}, respectively, indicating that the α-Fe$_2$O$_3$@C composite has a mesoporous structure. During the carbonization process of organic matter PDDA, the organic matter can be used as pore-forming agent to increase the pore size by the generation of bubbles [33]. The BET specific area of α-Fe$_2$O$_3$@C sample is ~4.66 m^2 g^{-1}. A large surface area can increase the contact area of electrolyte/electrode and reduce the current density per unit surface area during the electrode reaction process [34]. Moreover, the large specific area and pore diameter can promote the diffusion and mass transfer of the electrolyte. The internal pores of the electrode material can be used as active sites for charge storage, improving the capacitance properties of the electrode material [35,36].

To evaluate the properties of the α-Fe$_2$O$_3$@C sample as supercapacitors electrodes, we performed CV (-1.05–(-0.3 V)) and galvanostatic charge-discharge (-1.0–(-0.3 V)) measurements. According to the Randles Sevcik equation [37,38], if taking the peak current values of CV curves and plotting logarithm of peak current values versus logarithm of scan rate, the slope is ~0.75, indicating that the α-Fe$_2$O$_3$@C mainly shows double-layer capacitance and pseudocapacitive behavior. Therefore, this system could be described as a supercapacitor.

The CV curves of α-Fe$_2$O$_3$@C exhibit a pair of typical redox peak, indicating good faradaic reactions at the electrode surface with the pseudocapacitance charging mechanism. The anodic oxidation peak corresponds to the oxidation of Fe^{2+} to Fe^{3+} and the cathodic peak corresponds to the reduction of Fe^{3+} to Fe^{2+} [39,40]. With the scanning rate increasing, the potential difference between the anodic and the cathodic peak in the CV curve does not change too much. This indicates a good electrochemical reversibility of α-Fe$_2$O$_3$@C electrode material, which results from the kinetics of the interfacial faradaic redox reactions as well as the rapid electron transport [41].
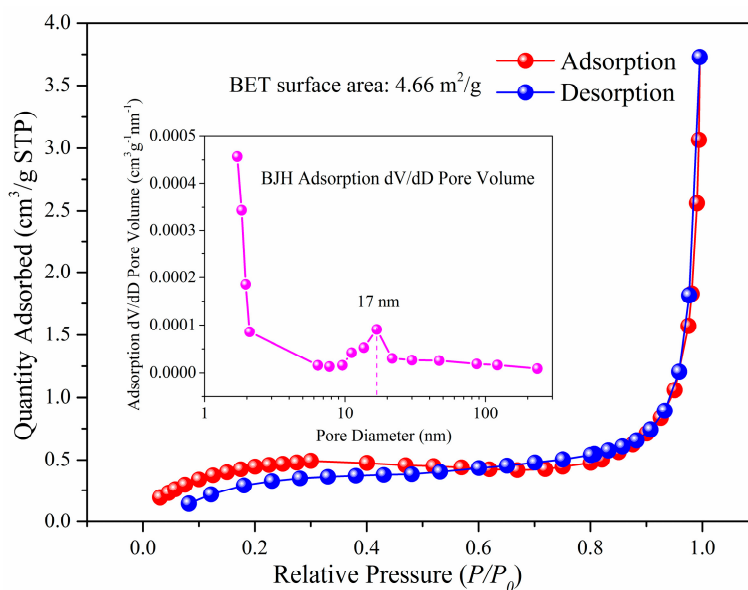
Figure 7. N_2 adsorption-desorption isotherm of α-Fe_2O_3@C nanoparticle composite. The insert is BJH pore size distribution.

As can be seen from Figure 8b, the discharge branch consists of two parts. The voltage drops quickly at the beginning of the discharge curve and is then followed by a slow decay, which is related to the capacitance and internal resistance of the electrode [42]. For the Fe_2O_3@C electrode, there is a combination of and Faraday capacitance and electric double layer capacitance, with a Faraday charge transfer and associated with electric double-layer charge transfer, resulting in longer discharge duration.

The mass specific capacitances (C) were calculated by equation $C = (I \times \Delta t)/(m \times \Delta V)$ where I is the constant discharge current (A), Δt is the discharging time (s), m is the mass of active electrode material α-Fe_2O_3@C (g), and ΔV is the voltage drop upon discharging (V). The value of capacitances are 406.9, 354.4, 304.9, 272.6, 224.3, and 162.8 Fg^{-1} at current densities of 0.5, 1.0, 2.0, 5.0, 10.0, and 20.0 Ag^{-1}, respectively.

The cycling life is an important indicator of the performance of supercapacitors, therefore the cycling stability of α-Fe_2O_3@C was investigated by repeating the charge-discharge tests at a high current density of 10 Ag^{-1} for 2000 cycles. It is found that after 2000 cycles, the specific capacitance of α-Fe_2O_3@C electrode material is 191.3 Fg^{-1} by remaining 90.7% of its initial specific capacitance (210.8 Fg^{-1}). In addition, the last 10 charge-discharge cycles at a current density of 10 Ag^{-1} demonstrate a stable and reversible characteristic without obvious downward trend. This may be due to the sandwich structure of α-Fe_2O_3@C electrode. The electrode material is not easy to fall off, and both sides of the Ni foam current collector are easy to charge conduction.

According to the literature [43], nickel foam also has a certain specific capacitance. In order to avoid the interference of Ni foam, CV (-1.0–(-0.3 V)) and galvanostatic charge–discharges (-1.0–(-0.3 V)) were performed in a three-electrode cell equipped with a piece of Ni foam (1 cm × 1 cm) as working electrode (without any active electrode material loaded on this Ni foam). The results were shown in Figure S2. The values of capacitances of blank Ni foam are 1.17, 0.94, and 0.81 Fg^{-1} at current densities of 0.1, 0.2, and 0.5 Ag^{-1}, respectively. The specific capacitance of the blank Ni foam is rather small, indicating that the excellent specific capacitance performance is mainly derived from the α-Fe_2O_3@C electrode material.

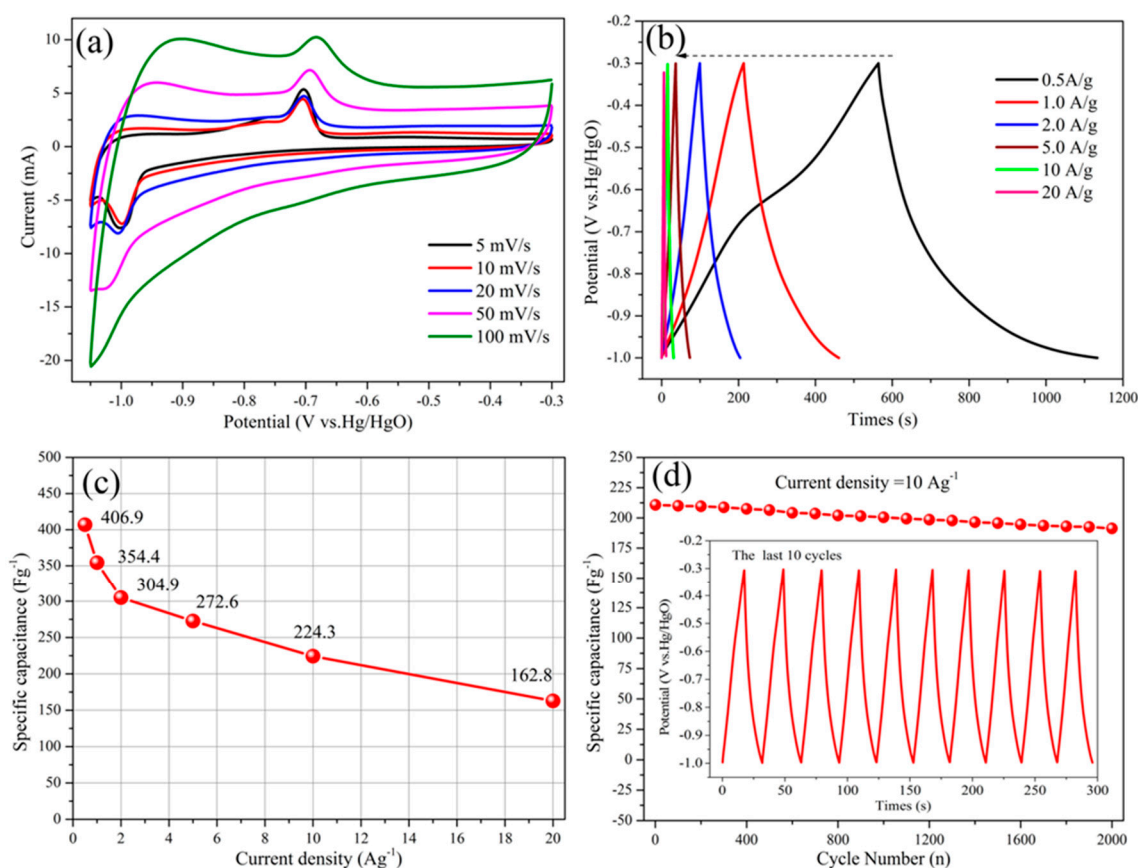**Figure 8.** (**a**) CV curves of α-Fe_2O_3@C electrodes at different scan rate; (**b**) charge-discharge curves of α-Fe_2O_3@C electrodes at different current density; (**c**) the specific capacitance of α-Fe_2O_3@C electrodes at different current densities; (**d**) cycling stability of α-Fe_2O_3@C electrodes at the current density of 10 Ag^{-1}, the insert is the last 10 charge-discharge cycles.

Table 1 summarizes some results of Fe_2O_3-based material used as supercapacitor electrodes in recent reports. It is also noted that our result in this paper exhibits higher specific capacitance than those reported in the literature at the corresponding current density. This excellent capacitive performance may be due to the fact that this unique carbon coating structure maintains the rapid transmission of electrolyte ions and electrons across the electrode, which efficiently utilizes pseudo-layers and double-layer capacitance to effectively improve the electrochemical performance of Fe_2O_3 electrode material [44,45]. This outstanding capacitance performance enables the α-Fe_2O_3@C nanocomposites to be promising electrode materials for next-generation energy storage and conversion devices.

The EIS behaviors of Fe_2O_3@C sandwich structure working electrode were further investigated (Figure S3). The Nyquist plots in the high frequency region show low internal resistance with a small equivalent series resistance (<0.1 Ω, the inset of Figure S3), due to the carbon coating improves the conductivity of the Fe_2O_3 material. In the low frequency region, the Nyquist plots exhibit a straight line, representing the diffusion limited electron transfer process of Fe_2O_3@C electrode.

Table 1. Comparison of Fe_2O_3-based electrode reported in recent literature using three-electrode system for supercapacitor applications.

Fe_2O_3-Based Electrode	Synthesis Method	Electrolyte	Potential Range (V)	Specific Capacitance $(Fg^{-1})/(Ag^{-1})$	Reference (year)
Fe_2O_3-graphene	solution-based hydrothermal	2 M KOH	−0.85–0	151.8/1.0 94/16	[46] (2012)
Porous α-Fe_2O_3	Sol-gel route	0.5 M Na_2SO_3	−0.8–0	193/1.0 90/5.0	[47] (2013)
g-C_3N_4/α-Fe_2O_3	ionic liquid assisted solvothermal	2.5 M Li_2SO_4	−1–0	260/0.5 87/5.0	[20] (2014)
N-doped grphene/Fe_2O_3	hydrothermal	1 M Na_2SO_4	−0.85–(−0.1)	260.1/2.0 145.1/5.0	[48] (2014)
N-rGO/Fe_2O_3	hydrothermal	1 M KOH	−1~0	268.4/2.0 137/5.0	[17] (2015)
α-Fe_2O_3	Template method	6 M KOH	−1.2–(−0.5)	330/0.5	[49] (2016)
Fe_2O_3 NDs@N-graphene	one-pot solvothermal	2 M KOH	−1.0–0	274/1.0 201/5.0	[50] (2016)
Fe_2O_3@MnO_2	two-step method	3 M KOH	−0.4–0.4	289.9/1.0 118.3/5.0	[40] (2017)
Fe_2O_3@C-rGO	hydrothermal	1 M Na_2SO_4	−0.5–0.5	211.4/0.5 177.2/20	[51] (2017)
α-Fe_2O_3 NTs/rGO	hydrothermal	1 M Na_2SO_4	−0.8–0	262/1.0 196.3/5.0	[52] (2017)
Fe_2O_3@C	hydrothermal self-assembly	6 M KOH	−1.0–(−0.3)	304.9/2.0 162.8/20	This work

As shown in Figure S4a,b, the nickel foam has a homogeneous porous structure, which facilitates the separation of the electrolyte and electrons. The pore size is about 200 nm. Before the cycling, the Fe_2O_3@C nanospheres, acetylene black and polytetrafluoroethylene (PTFE) are evenly distributed. The linear object is the binder (PTFE). After the cycling, the Fe_2O_3@C nanospheres morphology remain intact, with no significant expansion and rupture, which is due to the protective effect of carbon coating. Generally, the structure of Fe_2O_3 particles will break and collapse during the cycling process. The morphology and structure of Fe_2O_3@C sample were almost unchanged and still maintained the cocoon-shaped oval spherical structure. This further illustrated that the carbon coating can effectively buffer the volume expansion of Fe_2O_3 material to maintain structural stability and improve electrical properties [53].

4. Conclusions

In conclusion, we have successfully synthesized cocoon-like α-Fe_2O_3@C nanocomposites with a novel carbon-coated core-shell structure via a simple one-step hydrothermal self-assembly method and employed it as supercapacitor electrode material. The coating carbon layer improves the conductivity of α-Fe_2O_3 and also buffers its volume change during cycling. The porous structure of α-Fe_2O_3@C provides more active sites for charge storage, which effectively enhance the specific capacitance, cycling stability, and rate performance of α-Fe_2O_3. This one-step synthesis method is simple and efficient. It is suited for the large-scale production of other carbon-coated metal oxide materials. This cocoon-like α-Fe_2O_3 nanoparticle with a novel carbon-coated structure has potential for energy storage applications.

References

1. Wang, G.; Zhang, L.; Zhang, J. A review of electrode materials for electrochemical supercapacitors. *Chem. Soc. Rev.* **2012**, *41*, 797–828. [CrossRef] [PubMed]

2. Nithya, V.D.; Arul, N.S. Review on α-Fe$_2$O$_3$ based negative electrode for high performance supercapacitors. *J. Power Sources* **2016**, *327*, 297–318. [CrossRef]

3. Xiong, G.; Meng, C.; Reifenberger, R.G.; Irazoqui, P.P.; Fisher, T.S. Graphitic Petal Electrodes for All-Solid-State Flexible Supercapacitors. *Adv. Energy Mater.* **2013**, *4*, 1300515. [CrossRef]

4. Xiang, D.; Yin, L.; Wang, C.; Zhang, L. High electrochemical performance of RuO$_2$–Fe$_2$O$_3$ nanoparticles embedded ordered mesoporous carbon as a supercapacitor electrode material. *Energy* **2016**, *106*, 103–111. [CrossRef]

5. Peng, X.; Peng, L.; Wu, C.; Xie, Y. Two dimensional nanomaterials for flexible supercapacitors. *Chem. Soc. Rev.* **2014**, *43*, 3303–3323. [CrossRef] [PubMed]

6. Shivakumara, S.; Penki, T.R.; Munichandraiah, N. High specific surface area α-Fe$_2$O$_3$ nanostructures as high performance electrode material for supercapacitors. *Mater. Lett.* **2014**, *131*, 100–103. [CrossRef]

7. Lin, F.; Li, X.; Zhao, Y.; Yang, Z. Control Strategies with Dynamic Threshold Adjustment for Supercapacitor Energy Storage System Considering the Train and Substation Characteristics in Urban Rail Transit. *Energies* **2016**, *9*, 257. [CrossRef]

8. Baughman, R.H.; Zakhidov, A.A.; De Heer, W.A. Carbon Nanotubes—The Route Toward Applications. *Science* **2002**, *297*, 787–792. [CrossRef] [PubMed]

9. Wu, Z.S.; Zhou, G.; Yin, L.C.; Ren, W.; Li, F.; Cheng, H.-M. Graphene/metal oxide composite electrode materials for energy storage. *Nano Energy* **2012**, *1*, 107–131. [CrossRef]

10. Nan, H.; Yu, L.; Ma, W.; Geng, B.; Zhang, X. Flexible superior electrode architectures based on three-dimensional porous spinous α-Fe$_2$O$_3$ with a high performance as a supercapacitor. *Dalton Trans.* **2015**, *44*, 9581–9587. [CrossRef] [PubMed]

11. Zheng, X.; Han, Z.; Chai, F.; Qu, F.; Xia, H.; Wu, X. Flexible heterostructured supercapacitor electrodes based on α-Fe$_2$O$_3$ nanosheets with excellent electrochemical performances. *Dalton Trans.* **2016**, *45*, 12862–12870. [CrossRef] [PubMed]

12. Wang, Z.; Liu, C.J. Preparation and application of iron oxide/graphene based composites for electrochemical energy storage and energy conversion devices: Current status and perspective. *Nano Energy* **2015**, *11*, 277–293. [CrossRef]

13. Wang, L.; Yang, H.; Liu, X.; Zeng, R.; Li, M.; Huang, Y.; Hu, X. Constructing Hierarchical Tectorum-like α-Fe$_2$O$_3$/PPy Nanoarrays on Carbon Cloth for Solid-State Asymmetric Supercapacitors. *Angew. Chem. Int. Ed.* **2017**, *129*, 1125–1130. [CrossRef]

14. Yang, X.; Sun, H.; Zhang, L.; Zhao, L.; Lian, J.; Jiang, Q. High Efficient Photo-Fenton Catalyst of α-Fe$_2$O$_3$/MoS$_2$ Hierarchical Nanoheterostructures: Reutilization for Supercapacitors. *Sci. Rep.* **2016**, *6*, 31591. [CrossRef] [PubMed]

15. Liu, S.; Sun, S.; You, X. Inorganic nanostructured materials for high performance electrochemical supercapacitors. *Nanoscale* **2014**, *6*, 2037–2045. [CrossRef] [PubMed]

16. Gao, Y.; Wu, D.; Wang, T.; Jia, D.; Xia, W.; Lv, Y.; Cao, Y.; Tan, Y.; Liu, P. One-step solvothermal synthesis of quasi-hexagonal Fe$_2$O$_3$ nanoplates/graphene composite as high performance electrode material for supercapacitor. *Electrochim. Acta* **2016**, *191*, 275–283. [CrossRef]

17. Liu, H.D.; Zhang, J.L.; Xu, D.D.; Huang, L.H.; Tan, S.Z.; Mai, W.J. Easy one-step hydrothermal synthesis of nitrogen-doped reduced graphene oxide/iron oxide hybrid as efficient supercapacitor material. *J. Solid State Electrochem.* **2014**, *19*, 135–144. [CrossRef]

18. Yu, W.; Zhang, L.; Hou, P.; Li, F.; Liu, C.; Cheng, H. High Reversible Lithium Storage Capacity and Structural Changes of Fe$_2$O$_3$ Nanoparticles Confined inside Carbon Nanotubes. *Adv. Energy Mater.* **2016**, *6*, 1501755. [CrossRef]

19. Wang, S.; Hu, L.; Hu, Y.; Jiao, S. Conductive polyaniline capped Fe$_2$O$_3$ composite anode for high rate lithium ion batteries. *Mater. Chem. Phys.* **2014**, *146*, 289–294. [CrossRef]

20. Xu, L.; Xia, J.; Xu, H.; Yin, S.; Wang, K.; Huang, L.; Wang, L.; Li, H. Reactable ionic liquid assisted solvothermal synthesis of graphite-like C$_3$N$_4$ hybridized α-Fe$_2$O$_3$ hollow microspheres with enhanced supercapacitive performance. *J. Power Sources* **2014**, *245*, 866–874. [CrossRef]

21. Shou, Q.; Cheng, J.; Zhang, L.; Nelson, B.J.; Zhang, X. Synthesis and characterization of a nanocomposite of goethite nanorods and reduced graphene oxide for electrochemical capacitors. *J. Solid State Chem.* **2012**, *185*, 191–197. [CrossRef]

22. Xiang, Q.; Yu, J.; Jaroniec, M. Preparation and Enhanced Visible-Light Photocatalytic H$_2$-Production Activity of Graphene/C$_3$N$_4$ Composites. *J. Phys. Chem. C* **2011**, *115*, 7355–7363. [CrossRef]

23. Meher, S.K.; Justin, P.; Rao, G.R. Microwave-mediated synthesis for improved morphology and pseudocapacitance performance of nickel oxide. *ACS Appl. Mater. Interfaces* **2011**, *3*, 2063–2073. [CrossRef] [PubMed]

24. Dong, X.; Li, L.; Zhao, C.; Liu, H.-K.; Guo, Z. Controllable synthesis of RGO/Fe$_x$O$_y$ nanocomposites as high-performance anode materials for lithium ion batteries. *J. Mater. Chem. A* **2014**, *2*, 9844–9850. [CrossRef]

25. Cao, K.; Jiao, L.; Liu, H.; Liu, Y.; Wang, Y.; Guo, Z.; Yuan, H. 3D Hierarchical Porous α-Fe$_2$O$_3$ Nanosheets for High-Performance Lithium-Ion Batteries. *Adv. Energy Mater.* **2014**, *5*, 1401421. [CrossRef]

26. Sun, Z.; Yuan, H.; Liu, Z.; Han, B.; Zhang, X. A Highly Efficient Chemical Sensor Material for H$_2$S: α-Fe$_2$O$_3$ Nanotubes Fabricated Using Carbon Nanotube Templates. *Adv. Mater.* **2005**, *17*, 2993–2997. [CrossRef]

27. Wang, X.; Zhang, M.; Liu, E.; He, F.; Shi, C.; He, C.; Li, J.; Zhao, N. Three-dimensional core-shell Fe$_2$O$_3$@carbon/carbon cloth as binder-free anode for the high-performance lithium-ion batteries. *Appl. Surf. Sci.* **2016**, *390*, 350–356. [CrossRef]

28. Ma, C.; Zhang, W.; He, Y.S.; Gong, Q.; Che, H.; Ma, Z.F. Carbon coated SnO$_2$ nanoparticles anchored on CNT as a superior anode material for lithium-ion batteries. *Nanoscale* **2016**, *8*, 4121–4126. [CrossRef] [PubMed]

29. Guo, Q.; Qin, X. Flower-like SnO$_2$ nanoparticles grown on graphene as anode materials for lithium-ion batteries. *J. Solid State Electrochem.* **2013**, *18*, 1031–1039. [CrossRef]

30. Subramaniyam, C.M.; Islam, M.M.; Akhter, T.; Cardillo, D.; Konstantinov, K.; Liu, H.K.; Dou, S.X. A chemically modified graphene oxide wrapped porous hematite nano-architecture as a high rate lithium-ion battery anode material. *RSC Adv.* **2016**, *6*, 82698–82706. [CrossRef]

31. Hu, J.; Zheng, J.; Tian, L.; Duan, Y.; Lin, L.; Cui, S.; Peng, H.; Liu, T.; Guo, H.; Wang, X.; et al. A core-shell nanohollow-γ-Fe$_2$O$_3$@graphene hybrid prepared through the Kirkendall process as a high performance anode material for lithium ion batteries. *Chem. Commun.* **2015**, *51*, 7855–7858. [CrossRef] [PubMed]

32. Wang, H.; Xu, Z.; Yi, H.; Wei, H.; Guo, Z.; Wang, X. One-step preparation of single-crystalline Fe$_2$O$_3$ particles/graphene composite hydrogels as high performance anode materials for supercapacitors. *Nano Energy* **2014**, *7*, 86–96. [CrossRef]

33. Qin, X.; Zhang, H.; Wu, J.; Chu, X.; He, Y.-B.; Han, C.; Miao, C.; Wang, S.; Li, B.; Kang, F. Fe$_3$O$_4$ nanoparticles encapsulated in electrospun porous carbon fibers with a compact shell as high-performance anode for lithium ion batteries. *Carbon* **2015**, *87*, 347–356. [CrossRef]

34. Huang, Y.; Lin, Z.; Zheng, M.; Wang, T.; Yang, J.; Yuan, F.; Lu, X.; Liu, L.; Sun, D. Amorphous Fe$_2$O$_3$ nanoshells coated on carbonized bacterial cellulose nanofibers as a flexible anode for high-performance lithium ion batteries. *J. Power Sources* **2016**, *307*, 649–656. [CrossRef]

35. Li, Y.; Zhu, C.; Lu, T.; Guo, Z.; Zhang, D.; Ma, J.; Zhu, S. Simple fabrication of a Fe$_2$O$_3$/carbon composite for use in a high-performance lithium ion battery. *Carbon* **2013**, *52*, 565–573. [CrossRef]

36. Mai, L.Q.; Yang, F.; Zhao, Y.L.; Xu, X.; Xu, L.; Luo, Y.Z. Hierarchical MnMoO$_4$/CoMoO$_4$ heterostructured nanowires with enhanced supercapacitor performance. *Nat. Commun.* **2011**, *2*. [CrossRef] [PubMed]

37. Kant, R. Theory for staircase voltammetry and linear scan voltammetry on fractal electrodes: Emergence of anomalous Randles-Sevcik behavior. *Electrochim. Acta* **2013**, *111*, 223–233.

38. Mundinamani, S.P.; Rabinal, M.K. Molecular modification of highly degenerate semiconductor as an active electrode to enhance the performance of supercapacitors. *Mater. Res. Express* **2014**, *1*, 045508. [CrossRef]

39. Nie, G.; Lu, X.; Lei, J.; Jiang, Z.; Wang, C. Electrospun V$_2$O$_5$-doped α-Fe$_2$O$_3$ composite nanotubes with tunable ferromagnetism for high-performance supercapacitor electrodes. *J. Mater. Chem. A* **2014**, *2*, 15495–15501. [CrossRef]

40. Nie, G.; Lu, X.; Chi, M.; Zhu, Y.; Yang, Z.; Song, N.; Wang, C. Hierarchical α-Fe$_2$O$_3$@MnO$_2$ core-shell nanotubes as electrode materials for high-performance supercapacitors. *Electrochim. Acta* **2017**, *231*, 36–43. [CrossRef]

41. Li, J.J.; Liu, M.C.; Kong, L.B.; Wang, D.; Hu, Y.M.; Han, W.; Kang, L. Advanced asymmetric supercapacitors based on Ni$_3$(PO$_4$)$_2$@GO and Fe$_2$O$_3$@GO electrodes with high specific capacitance and high energy density. *RSC Adv.* **2015**, *5*, 41721–41728. [CrossRef]

42. Tian, W.; Wang, X.; Zhi, C.; Zhai, T.; Liu, D.; Zhang, C.; Golberg, D.; Bando, Y. Ni(OH)$_2$ nanosheet@Fe$_2$O$_3$ nanowire hybrid composite arrays for high-performance supercapacitor electrodes. *Nano Energy* **2013**, *2*, 754–763. [CrossRef]

43. Xing, W.; Qiao, S.; Wu, X.; Gao, X.; Zhou, J.; Zhuo, S.; Hartono, S.B.; Hulicova-Jurcakova, D. Exaggerated capacitance using electrochemically active nickel foam as current collector in electrochemical measurement. *J. Power Sources* **2011**, *196*, 4123–4127. [CrossRef]

44. Zhu, X.; Zhu, Y.; Murali, S.; Stoller, M.D.; Ruoff, R.S. Nanostructured Reduced Graphene Oxide/Fe$_2$O$_3$ Composite As a High-Performance Anode Material for Lithium Ion Batteries. *ACS Nano* **2011**, *5*, 3333–3338. [CrossRef] [PubMed]

45. Fan, Z.; Yan, J.; Zhi, L.; Zhang, Q.; Wei, T.; Feng, J.; Zhang, M.; Qian, W.; Wei, F. A three-dimensional carbon nanotube/graphene sandwich and its application as electrode in supercapacitors. *Adv. Mater.* **2010**, *22*, 3723–3728. [CrossRef] [PubMed]

46. Wang, D.; Li, Y.; Wang, Q.; Wang, T. Nanostructured Fe$_2$O$_3$-graphene composite as a novel electrode material for supercapacitors. *J. Solid State Electrochem.* **2011**, *16*, 2095–2102. [CrossRef]

47. Shivakumara, S.; Penki, T.R.; Munichandraiah, N. Preparation and electrochemical performance of porous hematite (α-Fe$_2$O$_3$) nanostructures as supercapacitor electrode material. *J. Solid State Electrochem.* **2013**, *18*, 1057–1066. [CrossRef]

48. Zhao, P.; Li, W.; Wang, G.; Yu, B.; Li, X.; Bai, J.; Ren, Z. Facile hydrothermal fabrication of nitrogen-doped graphene/Fe$_2$O$_3$ composites as high performance electrode materials for supercapacitor. *J. Alloys Compd.* **2014**, *604*, 87–93. [CrossRef]

49. Li, J.; Zhang, W.; Zan, G.; Wu, Q. A high-performance dual-function material: Self-assembled super long α-Fe$_2$O$_3$ hollow tubes with multiple heteroatom (C-, N- and S-) doping. *Dalton Trans.* **2016**, *45*, 12790–12799. [CrossRef] [PubMed]

50. Liu, L.; Lang, J.; Zhang, P.; Hu, B.; Yan, X. Facile Synthesis of Fe$_2$O$_3$ Nano-Dots@Nitrogen-Doped Graphene for Supercapacitor Electrode with Ultralong Cycle Life in KOH Electrolyte. *ACS Appl. Mater. Interfaces* **2016**, *8*, 9335–9344. [CrossRef] [PubMed]

51. Zhang, M.; Sha, J.; Miao, X.; Liu, E.; Shi, C.; Li, J.; He, C.; Li, Q.; Zhao, N. Three-dimensional graphene anchored Fe$_2$O$_3$@C core-shell nanoparticles as supercapacitor electrodes. *J. Alloys Compd.* **2017**, *696*, 956–963. [CrossRef]

52. Nathan, D.M.G.T.; Boby, S.J.M. Hydrothermal preparation of hematite nanotubes/reduced graphene oxide nanocomposites as electrode material for high performance supercapacitors. *J. Alloys Compd.* **2017**, *700*, 67–74. [CrossRef]

53. Wang, D.; Dong, H.; Zhang, H.; Zhang, Y.; Xu, Y.; Zhao, C.; Sun, Y.; Zhou, N. Enabling a High Performance of Mesoporous α-Fe$_2$O$_3$ Anodes by Building a Conformal Coating of Cyclized-PAN Network. *ACS Appl. Mater. Interfaces* **2016**, *8*, 19524–19532. [CrossRef] [PubMed]